Nanoscale

Precision ladder-structured silver cluster assembly bridged by tetrazine linkers for highly sensitive and selective luminescence recognition of amino acids

Tsukasa Irie, [ID] †[a] Riki Nakatani,†[a] Sreelakshmi K. S.,[a] Ayumu Kondo,[a] Tokuhisa Kawawaki, [ID] [a] Shuntaro Takahashi, [ID] [b] Saikat Das [ID] *[a] and Yuichi Negishi [ID] *[a]

Silver nanoclusters merge atomically defined structures with intense, environment-responsive photoluminescence, yet their notorious lability in air and water has constrained real-world sensing. Here we convert fragility into a design principle by immobilizing a silver nanocluster motif inside a reticularly reinforced, recognition-active lattice. **TUS 9** is a ladder-structured silver cluster-assembled material built from bow-shaped Ag_{13} units that first organize into one-dimensional chains ("rails") and are then stitched laterally by rigid 3,6-di(4-pyridyl)-1,2,4,5-tetrazine linkers ("rungs"). Single-crystal X-ray diffraction reveals a monoclinic $C2/c$ framework in which argentophilic contacts and a mixed thiolate/trifluoroacetate ligand shell stabilize the cluster scaffold, while directional Ag–N coordination locks interchain registry. Bulk phase fidelity is confirmed by PXRD and XPS, and the ordered packing generates permanent microporosity. In water, **TUS 9** retains strong emission with a sensing-ready band at 377 nm (λ_{ex} = 295 nm), enabling selective luminescence quenching by basic amino acids. L-Lysine and L-arginine produce pronounced Stern–Volmer responses (K_{SV} = 891.7 and 540.1 M^{-1}) with detection limits of 407 and 162 µM, respectively, whereas acidic amino acids perturb the emission only weakly. The response is fully recyclable over 10 cycles and post-sensing XPS shows preserved coordination environments. This work demonstrates that electronically active linkers can simultaneously stabilize silver nanocluster frameworks against aqueous degradation and encode molecular selectivity, opening a modular route to robust, programmable luminescent sensors.

Introduction

Metal nanoclusters (NCs) occupy a distinctive size regime between isolated atoms and conventional nanoparticles, typically comprising a few to several dozen metal atoms with overall dimensions below ~3 nm.[1–18] In this ultrasmall domain, classical metallic band structures give way to molecule-like, quantized electronic states, endowing NCs with properties that are fundamentally different from both bulk metals and larger nanocrystals. Their atomically defined cores, discrete energy levels, and ligand-protected surfaces collectively generate intense size-dependent photoluminescence, rich redox activity, and exceptionally high surface reactivity.[19–21]

These attributes have positioned NCs as versatile functional materials across a broad spectrum of fields, including heterogeneous and homogeneous catalysis,[22,23] chemical and biological sensing,[24,25] optoelectronics,[26,27] bioimaging,[28,29] chiral recognition,[30,31] photodynamic therapy,[32,33] and environmental remediation.[34,35] The extraordinary behavior of NCs originates from their precise structural organization at the atomic level. Unlike plasmonic nanoparticles, NCs exhibit well-resolved electronic transitions governed by metal–metal bonding, ligand–metal charge transfer, and quantum confinement effects. Their ligand shells not only stabilize the metal cores but also actively modulate electronic structure, surface accessibility, and interfacial interactions. As a result, subtle variations in cluster nuclearity, geometry, or ligand identity can translate into pronounced changes in photophysical, catalytic, and recognition properties. This intrinsic structure–property sensitivity renders NCs powerful platforms for molecular-level materials design. Among the diverse family of metal NCs, silver nanoclusters (Ag NCs) have attracted sustained interest due to their remarkable photoluminescence, flexible coordination chemistry, and ability to adopt a wide variety of nuclea-

[a]*Institute of Multidisciplinary Research for Advanced Materials, Tohoku University, Aoba-ku, Sendai 980-8577, Japan. E-mail: das.saikat.c4@tohoku.ac.jp, yuichi.negishi.a8@tohoku.ac.jp*

[b]*Chemical Materials Development Department, TANAKA PRECIOUS METAL TECHNOLOGIES Co., Ltd, Tsukuba Technical Center, 22 Wadai, Tsukuba, Ibaraki 300-4247, Japan*

† These authors contributed equally.

rities and structural motifs.[36–40] Ag NCs frequently display strong metal-centered and metal-to-ligand electronic transitions, producing bright and tunable emission that is highly sensitive to the local chemical environment. In addition, Ag(I) ions readily form multinuclear assemblies with soft donor ligands, enabling the construction of architecturally diverse cluster cores ranging from compact polyhedra to extended chain-like motifs. Despite these attractive features, the practical use of Ag NCs has long been impeded by their limited chemical robustness. The relatively labile nature of Ag–ligand coordination, combined with the high surface exposure of silver atoms in ultrasmall clusters, renders them susceptible to oxidation, photodegradation, and structural rearrangement under ambient conditions. Moisture, oxygen, and light can readily disrupt Ag–S, Ag–N, or Ag–P bonds, leading to cluster fragmentation, aggregation, or loss of luminescence. This intrinsic vulnerability has restricted the deployment of Ag NCs in real-world sensing, catalytic, and biomedical applications, where long-term stability in aqueous or photochemically active environments is essential.

In response to these limitations, the field has increasingly embraced extended silver cluster-based architectures. By organizing Ag NCs into higher-order assemblies, it becomes possible to suppress undesirable structural dynamics, reduce surface exposure, and introduce cooperative stabilization through inter-cluster interactions.[41–43] While early efforts relied primarily on non-covalent self-assembly, such approaches often suffer from limited structural predictability, weak intermolecular cohesion, and poor control over framework topology.[44,45] In contrast, reticular chemistry[46] provides a powerful and transformative design paradigm for organizing metal NCs into crystalline, long-range ordered networks. By linking well-defined inorganic nodes with multitopic organic ligands through directional coordination bonds, reticular strategies enable the deliberate construction of materials with precise connectivity, tunable dimensionality, and programmable topology. Within this framework, silver cluster-assembled materials (SCAMs) have emerged as a unique class of crystalline solids in which multinuclear Ag(I) clusters serve as secondary building units, interconnected by organic linkers to form extended architectures reminiscent of metal–organic frameworks (MOFs), yet distinguished by their cluster-derived electronic and photophysical characteristics.[47–50] The incorporation of multidentate organic linkers plays a central role in the success of SCAM design. Such linkers act as structural "molecular staples", anchoring multiple silver centers simultaneously and enforcing rigid spatial arrangements that suppress cluster mobility and degradation. Directional coordination between ligand donor sites and Ag cluster nodes promotes the formation of well-defined one-, two-, or three-dimensional (1D, 2D, or 3D) frameworks with controllable topologies, while the chemical modularity of the ligands enables systematic tuning of pore environments, surface functionalities, and electronic landscapes. Importantly, this structural rigidity not only enhances mechanical integrity but also stabilizes the delicate electronic states responsible for cluster-based luminescence, significantly improving photostability under operational conditions.

A landmark demonstration of this concept was reported by Zang and co-workers, who replaced labile surface ligands on Ag$_{12}$ NCs with rigid bipyridyl linkers to construct 2D silver cluster frameworks.[51] This reticular reorganization effectively immobilized the clusters, reduced their exposure to degradative agents, and produced materials that retained structural integrity and luminescence for over one year. Remarkably, the photoluminescence quantum yield increased to 12.1%, underscoring how precise spatial separation and controlled orientation of Ag clusters can enhance both stability and optical performance. This study established reticular chemistry as a viable strategy for transforming fragile Ag NCs into robust functional materials. Building on this foundation, a diverse library of SCAMs has since been developed using organic linkers such as pyrazines, azopyridines, porphyrins, imidazoles, carboxylates, thioureas, and spiro-based scaffolds.[52–59] These ligands have enabled the construction of silver cluster frameworks spanning 1D, 2D, and 3D architectures with tailored optical, electronic, and adsorption properties. In parallel, the range of accessible silver cluster nodes has expanded well beyond the prototypical Ag$_{12}$ core[60–64] to include Ag$_5$,[59] Ag$_9$,[65] Ag$_{10}$,[66] Ag$_{11}$,[67] Ag$_{14}$,[54] Ag$_{15}$,[68] Ag$_{20}$,[69] Ag$_{27}$,[70] and even Ag$_{72}$ clusters.[71] The combination of variable cluster nuclearity and ligand geometry provides a rich design space for tuning framework connectivity, pore environments, and photophysical behavior. Yet, despite the impressive structural diversity of SCAMs, their translation into solution-compatible functional materials—particularly for luminescence-based chemical sensing—remains limited. Many reported systems retain sensitivity to water, oxygen, or prolonged light exposure, restricting their practical use in biologically or environmentally relevant media. Achieving simultaneous framework robustness, strong emission, and selective molecular recognition under aqueous conditions continues to represent a major unresolved challenge.

Herein, we report a new SCAM, denoted **TUS 9**, that integrates structural robustness with highly selective luminescent sensing capability. Unlike conventional SCAMs built from discrete cluster nodes, **TUS 9** is composed of 1D chains of Ag$_{13}$ clusters that are laterally interconnected by 3,6-di(4-pyridyl)-1,2,4,5-tetrazine linkers. This unique organization generates a precision ladder-like architecture, in which the silver cluster chains form the rails and the tetrazine linkers serve as the rungs. The bidentate pyridyl termini of the tetrazine linkers establish strong and directional coordination with the Ag$_{13}$ clusters, conferring high structural rigidity and pronounced stability against hydrolytic and photochemical degradation. Simultaneously, the electron-deficient tetrazine core provides a chemically responsive recognition site within the framework. As a result, **TUS 9** maintains crystallinity and luminescence in aqueous environments—overcoming a long-standing limitation of silver cluster materials. Beyond stability, **TUS 9** exhibits pronounced and selective luminescence responses toward basic amino acids such as L-lysine and L-arginine, while dis-

playing minimal sensitivity toward acidic amino acids including L-aspartic acid and L-glutamic acid. This selectivity originates from the distinct molecular interactions between the tetrazine moieties and the functional groups of different amino acids. The protonated $-NH_3^+$ groups of lysine and arginine engage in strong hydrogen bonding and electrostatic interactions with the electron-poor nitrogen atoms of the tetrazine ring, facilitating efficient host–guest association and perturbation of the cluster-based electronic states responsible for emission. In contrast, the negatively charged $-COO^-$ groups of acidic amino acids introduce unfavorable electrostatic interactions with the tetrazine core, suppressing effective binding and minimizing luminescence modulation. This differential interaction mechanism enables **TUS 9** to function as a selective optical probe for basic amino acids in aqueous media, with high sensitivity, rapid response, and excellent recyclability (Fig. 1). The cooperative effects of framework rigidity, linker-directed recognition, and cluster-based photophysics collectively underpin the exceptional sensing performance of this system. More broadly, this work demonstrates how rational linker design within cluster-based reticular frameworks can

simultaneously enhance chemical stability and functional specificity. By integrating electronically active linkers into robust silver cluster architectures, it becomes possible to transcend the traditional trade-off between structural durability and molecular responsiveness. Such strategies open new avenues for the development of next-generation luminescent materials for chemical sensing, bioanalysis, and environmental monitoring.

Results and discussion

Structural genesis and reticular organization of TUS 9

The formation of **TUS 9** proceeds through a hierarchical assembly pathway in which preorganized silver–ligand motifs evolve into an extended, reticularly connected cluster framework. When polymeric $[AgStBu]_n$ is dispersed in an acetonitrile/ethanol mixture, the initial turbidity reflects the presence of aggregated thiolate-protected silver species. Introduction of CF_3COOAg induces a gradual clarification of the suspension, consistent with partial ligand redistribution
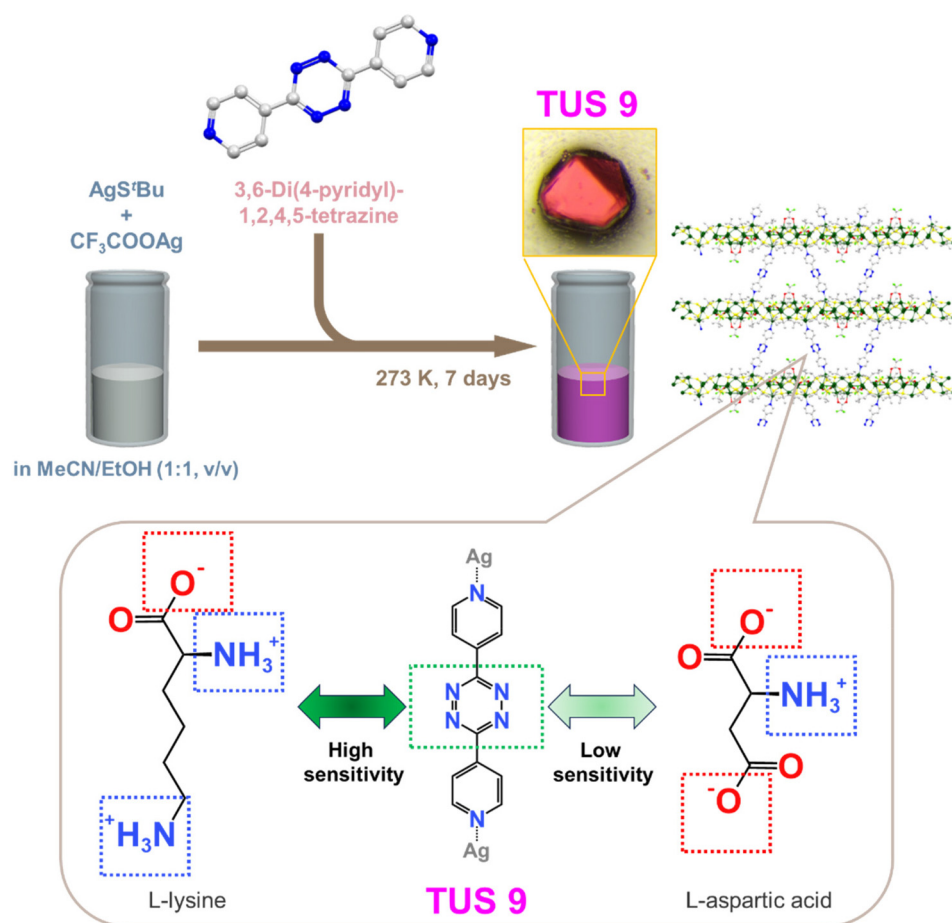

Fig. 1 Synthetic route and optical micrograph of **TUS 9**, highlighting the ladder-like arrangement of Ag_{13} cluster chains bridged by tetrazine linkers. The framework selectively responds to basic amino acids (L-lysine, L-arginine) through favorable host–guest interactions with tetrazine units, while acidic amino acids (L-aspartic acid, L-glutamic acid) show negligible effects.

and solubilization of multinuclear Ag(ɪ) clusters stabilized by a mixed thiolate–carboxylate shell. The trifluoroacetate anions, being more labile and oxygen-donating, weaken the original Ag–S network sufficiently to generate coordinatively accessible Ag sites while preserving the integrity of the nascent cluster core. This pre-equilibrated silver cluster solution provides a chemically adaptive platform for framework construction. Upon addition of 3,6-di(4-pyridyl)-1,2,4,5-tetrazine, directional coordination is initiated through the pyridyl nitrogen donors, which selectively bind to exposed Ag(ɪ) centers on the periphery of the preformed Ag_{13} cluster chains. The rigid, linear geometry of the linker enforces a well-defined interchain registry, aligning neighboring chains into an ordered ladder-like arrangement rather than allowing random aggregation. Slow diffusion and crystallization at 273 K allow this coordination-driven organization to proceed under thermodynamic control, ultimately yielding a long-range ordered, ladder-structured SCAM. After seven days, the reaction affords pink, truncated octahedral single crystals of **TUS 9** in high isolated yield (76% based on Ag). Optical microscopy reveals sharply faceted morphologies with uniform crystal habits, indicating coherent lattice propagation and minimal defect formation (Fig. 1). The well-defined crystal shape reflects the balance between the dynamic nature of Ag–ligand coordination and the stabilizing influence of the rigid tetrazine-based linkers, which collectively guide the system toward a single dominant packing motif.

Single-crystal X-ray diffraction (SCXRD) analysis establishes that **TUS 9** crystallizes in the monoclinic space group $C2/c$, revealing a precisely organized cluster framework constructed from one-dimensional (1D) chains of Ag_{13} NCs that are laterally interconnected by ditopic organic linkers. Structural dissection shows that the fundamental inorganic building block is an arched, bow-shaped Ag_{13} cluster (Fig. 2a and S2), whose geometry is defined by a central Ag2–Ag2 dimer forming the "crown", a basal Ag1 vertex, and two symmetric Ag3–Ag2–Ag4 wings that extend laterally. The crown and base are connected through Ag6 bridging units, generating a curved, three-tiered scaffold. The lateral wings further stabilize the architecture by distributing metal–metal interactions across the cluster periphery. The resulting configuration forms an open, distorted argentophilic framework with a pronounced bow-shaped topology rather than a closed polyhedral geometry. The average Ag–Ag separation of 3.033 Å, significantly shorter than the van der Waals contact distance for silver (3.44 Å), confirms the presence of substantial Ag⋯Ag interactions that reinforce cluster cohesion (Table S2).

The Ag_{13} core is enveloped by a protective ligand shell composed of ten *tert*-butylthiolate ligands and three trifluoroacetate anions. The thiolate ligands adopt multiple μ_2- and μ_3-bridging coordination modes, binding adjacent Ag atoms and weaving a flexible yet robust sulfur-rich network around the cluster surface (Fig. 2b and S3). The Ag–S bond distances span 2.387–2.796 Å, with an average of 2.561 Å (Table S3), consistent with strong Ag–S interactions that stabilize the metal core while preserving structural adaptability. Notably, individual
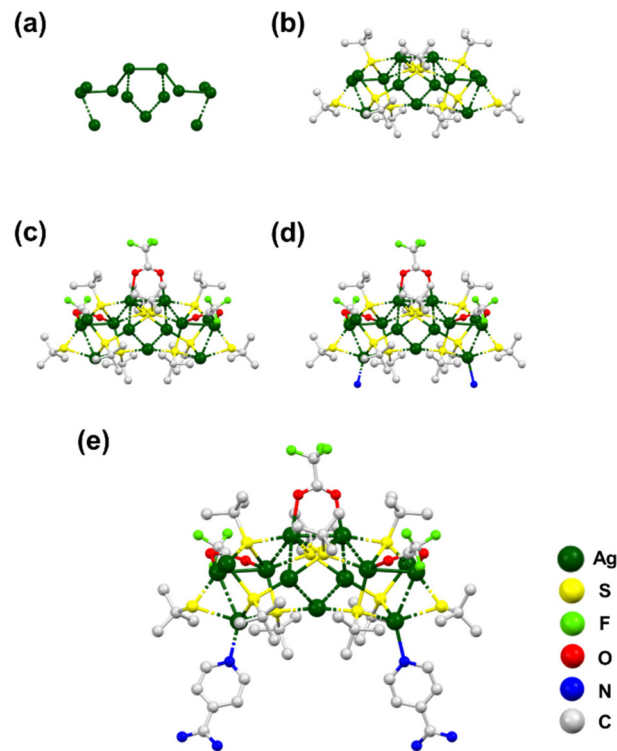

Fig. 2 Progressive assembly of the Ag_{13} cluster node in **TUS 9**: (a) Bow-shaped Ag_{13} metal core scaffold, (b) thiolate surface ligation, (c) incorporation of trifluoroacetate ligands, and (d) coordination of tetrazine-based linkers. (e) Fully ligated clusters organize into linear chains and are laterally interconnected by tetrazine bridges, generating the ladder-type framework. H atoms are omitted for clarity.

sulfur donors (S1–S5) participate in distinct coordination motifs: some bridge basal and wing Ag atoms, others cap peripheral sites, and several form chelating linkages that reinforce intermetallic connectivity. This diversity of binding modes allows the ligand shell to conform to the curved geometry of the Ag_{13} core without imposing excessive steric strain. Complementing the thiolate protection, the trifluoroacetate ligands bridge pairs of Ag atoms *via* bidentate *O,O′*-coordination (Fig. 2c and S4). The Ag–O distances (2.326–2.431 Å, average 2.365 Å; Table S4) indicate moderately strong coordination that contributes to charge balance and surface passivation. These oxygen donors predominantly occupy sites proximal to the crown region, further stabilizing the upper portion of the cluster while maintaining open coordination sites for framework propagation.

The extended architecture of **TUS 9** emerges through the bidentate coordination of the tetrazine linker's pyridyl termini to silver atoms located on the periphery of the preformed Ag_{13} cluster chains. Each linker binds two Ag centers in a near-linear fashion (average Ag–N distance = 2.212 Å; Table S5), functioning as a rigid molecular spacer that connects Ag_{13} clusters from neighboring chains (Fig. 2d, e and S5). Unlike flexible linkers that permit significant rotational freedom, the tetrazine backbone enforces a fixed spatial orientation, pro-

moting well-defined interchain alignment rather than random cross-linking. As a consequence, the Ag_{13} clusters first assemble into 1D chains through metal–metal and ligand-mediated interactions, with successive cluster units arranged in a head-to-tail fashion. These chains constitute the "rails" of the ladder motif. Orthogonal to this direction, tetrazine linkers bridge adjacent chains laterally, forming the "rungs" that lock the framework into a ladder-like topology (Fig. 3). Each linker thus acts as a linear ditopic connector that not only links neighboring chains but also defines the interchain separation and overall framework geometry. The resulting network exhibits a periodic arrangement of parallel Ag_{13} chains, with tetrazine bridges establishing uniform spacing and long-range structural coherence across the lattice. This hierarchical organization—clusters → chains → ladders—distinguishes **TUS 9** from conventional SCAMs constructed from discrete cluster nodes and underscores the critical role of linker rigidity and directionality in shaping framework topology. The ordered packing of these ladder motifs generates accessible voids between adjacent chains, giving rise to permanent microporosity within the crystal lattice. Nitrogen adsorption–desorption measurements at 77 K reveal a Type-I isotherm with a steep uptake at low relative pressures ($P/P_0 < 0.01$), characteristic of microporous materials (Fig. 4e). The Brunauer–Emmett–Teller (BET) surface area of 85.4 m^2 g^{-1} (Fig. S6) reflects the presence of confined pore channels formed by the regular spacing of the ladder rails and rungs. Unlike porous frameworks built from rigid polyhedral cages, the porosity in **TUS 9** arises from the cooperative arrangement of elongated cluster chains and linear organic spacers, creating narrow, chemically heterogeneous adsorption sites decorated with both metal-rich surfaces and nitrogen-containing linker functionalities that are well suited for selective host–guest interactions.

Bulk phase integrity and chemical-state validation of TUS 9

The structural coherence of **TUS 9** beyond single crystals was first established by powder X-ray diffraction (PXRD). The PXRD pattern collected from the activated bulk sample reproduces
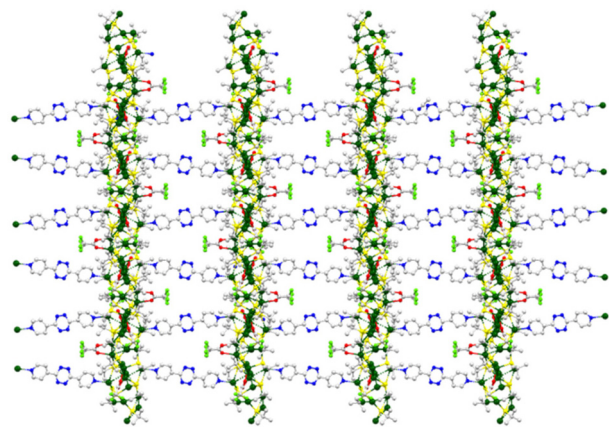

Fig. 3 Parallel Ag_{13} cluster chains are stitched together by tetrazine linkers to form the extended ladder-type architecture of **TUS 9**.

the principal Bragg reflections of the simulated diffractogram generated from the SCXRD model, confirming that the ladder-type architecture observed crystallographically is retained at the ensemble scale (Fig. 4a). The absence of parasitic reflections indicates negligible formation of competing crystalline byproducts, while the sharpness of the reflections supports high long-range order and phase homogeneity across the bulk material. To verify that the extended ladder framework is not merely crystallographically intact but also chemically faithful to the SCXRD-resolved composition, X-ray photoelectron spectroscopy (XPS) was employed to interrogate the surface elemental inventory and electronic states. The survey spectrum displays signals attributable to Ag, S, N, O, F, and C (Fig. 4b), consistent with a silver cluster chain protected by thiolate and trifluoroacetate ligands and cross-linked by the nitrogen-rich tetrazine/pyridyl linker. Importantly, the simultaneous presence of S (thiolate), N (linker), and O/F (trifluoroacetate) confirms that the bulk material preserves the multiligand shell and linker integration essential for chain formation and interchain stitching in **TUS 9**. High-resolution spectra provide a more discriminating picture of the coordination chemistry. In the Ag 3d region (Fig. S7a), the doublet at 367.7 eV (Ag $3d_{5/2}$) and 373.7 eV (Ag $3d_{3/2}$) with a spin–orbit separation of ~6.0 eV is characteristic of Ag(I) bound to soft donors (*e.g.*, thiolates) and N/O ligands in coordination frameworks. This assignment is consistent with the coordination environment revealed by SCXRD, in which silver atoms are bound by thiolate sulfur atoms, carboxylate oxygen atoms, and pyridyl nitrogen atoms, rather than forming metallic Ag(0). From an electronic-structure standpoint, Ag(I) is d^{10} and therefore closed-shell, which aligns with the diamagnetic, coordination-driven nature of the Ag centers in a ligand-stabilized cluster framework. The thiolate shell is clearly reflected in the S 2p region (Fig. S7d), which exhibits a spin–orbit split doublet centered at ~161.7 eV (S $2p_{3/2}$) and ~162.8 eV (S $2p_{1/2}$). These binding energies are diagnostic of thiolate (S^-) bound to Ag(I) rather than oxidized sulfur species; notably, no high-binding-energy components (typically >167 eV) are observed, indicating that the sulfur framework remains chemically reduced and that appreciable sulfoxide/sulfone formation does not occur during synthesis or handling. The O 1s spectrum (Fig. S7e) shows a dominant component at 531.1 eV, which is appropriately assigned to carboxylate oxygen atoms coordinated to Ag ($–COO^- → Ag$) in the trifluoroacetate ligands. (In many carboxylate systems, co-ordinated O appears near ~531–532 eV; adventitious/weakly bound oxygenated carbon species generally populate higher binding energies, often ~532.5–534 eV.) The observation of a strong, well-positioned O 1s feature therefore supports preservation of Ag–O coordination and the CF_3COO^- capping/bridging roles established crystallographically. The N 1s region (Fig. S7f) is particularly informative because the linker provides two chemically distinct nitrogen populations: pyridyl N donors (metal-binding) and tetrazine ring N atoms (electron-poor, non-metal-binding). Accordingly, the spectrum resolves two components at 398.4 eV and 400.1 eV. The lower-binding-energy peak at 398.4 eV is consistent with pyridyl nitrogen
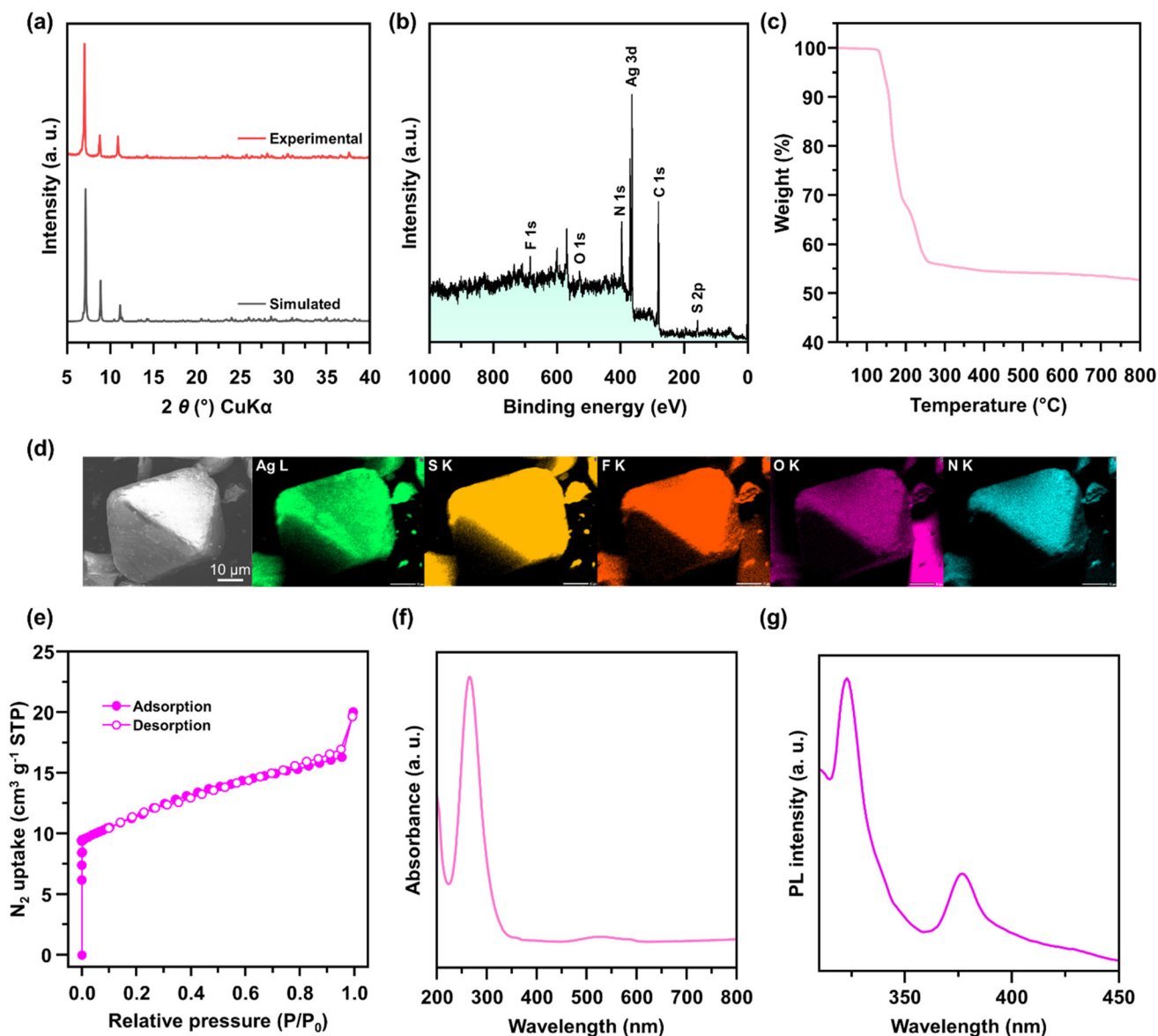
Fig. 4 Structural, compositional, and optical characterization of **TUS 9**: (a) comparison of experimental and simulated PXRD patterns verifying phase purity; (b) XPS survey spectrum showing surface elemental composition; (c) thermogravimetric profile illustrating thermal stability; (d) SEM image with corresponding EDX maps revealing homogeneous elemental distribution; (e) N_2 adsorption–desorption isotherms at 77 K demonstrating microporosity; (f) UV-vis absorption spectrum of **TUS 9** in water; and (g) photoluminescence emission spectrum in aqueous dispersion under 295 nm excitation.

engaged in Ag–N coordination, whereas the higher-binding-energy feature at 400.1 eV is reasonably attributed to the more electron-deficient tetrazine nitrogens within the aromatic N_4 core. This separation is chemically intuitive: coordination and intrinsic electron deficiency generate distinguishable N 1s environments, and together these peaks verify that the linker is incorporated in its intended dual role—pyridyl termini as coordination anchors and tetrazine as an electronically distinctive functionality embedded in the framework. Finally, the F 1s peak at 687.3 eV (Fig. S7c) confirms the presence of CF_3 groups, corroborating retention of the trifluoroacetate ligands in the bulk phase. Taken together, the XPS results validate not

only elemental composition but also the persistence of the key coordination motifs—Ag–S (thiolate shell), Ag–O (carboxylate binding), and Ag–N (pyridyl linkage)—required to sustain the Ag_{13}-chain/ladder architecture of **TUS 9**. Thermogravimetric analysis (TGA) further indicates that the framework remains intact up to *ca.* 135 °C under the measurement conditions (Fig. 4c), consistent with a coordination-assembled material stabilized by multidentate surface ligation and interchain linker bridging, yet expected to undergo ligand-related mass loss at elevated temperatures. Morphological analysis by SEM reveals well-developed, truncated octahedral crystals with smooth facets and uniform size distribution (Fig. 4d), matching the single-crystal habit

observed optically. Elemental mapping (EDX) shows spatially homogeneous distributions of Ag, S, F, O, and N across the crystal surface, supporting bulk compositional uniformity and excluding macroscopic phase segregation. Collectively, PXRD, XPS, SEM–EDX, and TGA converge to confirm that **TUS 9** is obtained as a phase-pure, chemically faithful, and structurally robust silver cluster-assembled ladder framework—an essential foundation for evaluating its luminescence response and aqueous sensing performance.

Optical fingerprints of TUS 9 in water: from electronic states to a sensing-ready emission handle

Because the ultimate function of **TUS 9** is luminescence recognition in water, its electronic structure was examined under conditions that mimic the sensing environment. In aqueous dispersion, **TUS 9** exhibits a pronounced UV absorption band centered at 266 nm (Fig. 4f). This feature is most reasonably assigned to ligand-centered $\pi \rightarrow \pi^*$ transitions dominated by the aromatic pyridyl rings and the tetrazine scaffold, with additional intensity enhancement arising from cluster–ligand electronic coupling at the Ag(I) coordination sites. In the ladder framework, the pyridyl termini are directly coordinated to Ag(I), and the tetrazine ring is electronically conjugated to these donors; thus, the 266 nm band reflects the "optical address" of the linker environment as embedded within the cluster-assembled lattice. Importantly, such high-energy absorptions are expected to remain observable in water because they originate from robust intraligand transitions that are comparatively insensitive to moderate dielectric changes. To further deconvolute framework *versus* linker contributions, solid-state diffuse reflectance UV-vis spectra were collected for **TUS 9** and the 3,6-di(4-pyridyl)-1,2,4,5-tetrazine linker (Fig. S8). **TUS 9** displays two prominent absorption features at 287 nm and 433 nm, whereas the free linker shows bands at 303 nm and 582 nm. The ~300 nm region in both spectra can be attributed to $\pi \rightarrow \pi^*$ transitions of the aromatic system (pyridyl and tetrazine-containing conjugation). The differences in peak position (287 nm in **TUS 9** *vs.* 303 nm in the free linker) are consistent with coordination-induced perturbation: binding of pyridyl nitrogens to Ag(I) alters electron density and orbital energies, leading to a shift in the high-energy absorption. The lower-energy bands provide deeper insight into how framework formation reshapes excited states. The linker's band at 582 nm is characteristic of an intramolecular charge-transfer (ICT) transition in an electron-deficient tetrazine chromophore conjugated with pyridyl donors. Upon incorporation into **TUS 9**, this low-energy absorption is strongly shifted to 433 nm, indicating that the framework environment substantially modifies the electronic landscape of the linker. Such a shift is consistent with coordination-enabled electronic coupling between the Ag(I) chain nodes and the linker, which can stabilize different frontier orbital distributions and alter charge-transfer energies. In other words, the linker does not behave as an isolated molecular chromophore once embedded in the ladder; instead, it becomes part of a coupled cluster–ligand electronic system.

Photoluminescence (PL) measurements on aqueous dispersions of **TUS 9** reveal two intense emission bands at 323 nm and 377 nm upon excitation at 295 nm (Fig. 4g). These emissions indicate the presence of at least two emissive channels, most plausibly arising from (i) a higher-energy ligand-dominated fluorescence component (near 323 nm) and (ii) a lower-energy emission (377 nm) that is more sensitive to the framework microenvironment and cluster–ligand coupling. The emergence of dual emission is consistent with a reticularly constrained Ag(I) cluster material in which ligand-based excited states coexist with framework-perturbed states that can involve ligand-to-metal/metal-to-ligand charge redistribution within the Ag(I)–N/S/O coordination manifold. Although the aqueous UV-vis spectrum shows a maximum at 266 nm, 295 nm excitation was selected because it more selectively populates the emissive manifold that yields the robust 377 nm band, while minimizing contributions from strongly absorbing high-energy transitions that can introduce inner-filter effects or enhanced scattering in turbid aqueous dispersions. Practically, excitation at 295 nm also provides a cleaner spectral baseline and avoids excessive overlap between excitation and emission channels, improving quantitative monitoring of the emission intensity during titrations. This choice becomes especially important for sensing, where small changes in emission intensity must be resolved reproducibly in water. For amino-acid recognition experiments, the emission intensity at 377 nm was therefore adopted as the analytical signal because it is (i) intense, (ii) well separated from excitation, and (iii) expected to be particularly responsive to local supramolecular interactions occurring within the linker-defined microenvironment of the ladder framework. Solid-state PL measurements further clarify how framework construction transforms optical output relative to the free linker. Under 287 nm excitation, both **TUS 9** and the tetrazine linker emit at 329 nm, but **TUS 9** exhibits markedly higher intensity (Fig. S9). This enhancement is consistent with rigidification-enhanced emission: embedding the linker within the reticular scaffold suppresses vibrational and torsional motions that otherwise promote nonradiative decay in the free molecule. In effect, the ladder framework acts as a structural clamp that preserves radiative pathways. Under 433 nm excitation, **TUS 9** displays a sharp emission at 657 nm, whereas the free linker shows a broader emission centered at 649 nm (Fig. S10). The appearance of a narrow, red emission in the framework at this excitation energy supports the presence of a well-defined lower-energy excited state stabilized by the ordered lattice—consistent with an ICT-like or framework-coupled emissive state that is more homogeneous in the crystalline environment than in the molecular solid of the free linker. The small red shift and spectral sharpening upon framework formation are both in line with an environment that imposes uniform conformations and well-regulated electronic coupling between chromophores and metal coordination sites.

Collectively, these absorption and emission signatures establish a clear photophysical foundation for aqueous sensing. First, **TUS 9** retains strong and trackable emission in

water, confirming that the ladder architecture protects the emissive states from rapid quenching or decomposition under aqueous conditions.

Second, the framework introduces emissive channels that are not simply those of the free linker, implying that the optical response can be modulated by analyte binding events that perturb the local electronic environment—particularly around the tetrazine/pyridyl region that is chemically positioned to interact with amino acids. Finally, the selection of the 377 nm band as a stable, high-contrast readout provides a quantitative handle for monitoring host–guest interactions in real time during titration experiments in water.

Selective luminescence recognition of amino acids in water

The ability to detect amino acids in aqueous environments is of broad scientific and technological relevance, spanning biomedical diagnostics, metabolic monitoring, food quality control, and environmental analysis. Variations in amino acid concentrations are closely linked to physiological disorders, microbial activity, and nutrient balance, motivating the development of optical probes that can operate directly in water with high sensitivity and molecular selectivity. From a materials-design perspective, such sensing requires a platform that combines (i) chemical robustness in aqueous media, (ii) accessible recognition sites for biomolecules, and (iii) emissive states that respond predictably to guest binding. The ladder-structured silver cluster assembly **TUS 9** fulfills these criteria through its rigid Ag_{13}-chain framework and its tetrazine-based linker environment, which together create a chemically differentiated, water-stable, and photophysically responsive host matrix. The selection of ʟ-lysine and ʟ-arginine as representative basic amino acids, and ʟ-aspartic acid and ʟ-glutamic acid as representative acidic amino acids, was guided by their contrasting charge states and functional group chemistries under physiological conditions. Lysine and arginine possess protonated $-NH_3^+$ groups (and in the case of arginine, a guanidinium moiety) that are strong hydrogen-bond donors and electrostatic partners. In contrast, aspartic acid and glutamic acid feature deprotonated $-COO^-$ side chains that introduce negative charge and reduced hydrogen-bond donation capability. This polarity contrast provides a chemically meaningful framework for probing how the tetrazine-rich microenvironment of **TUS 9** discriminates between cationic and anionic amino acid guests.

Upon incremental addition of ʟ-lysine (0.26–3.15 mM) to aqueous dispersions of **TUS 9** under excitation at 295 nm, a progressive and monotonic decrease in emission intensity was observed (Fig. 5a). The quenching behavior can be rationalized by specific host–guest interactions between the lysine molecules and the tetrazine-lined framework. The protonated $-NH_3^+$ group of lysine is well positioned to engage in hydrogen bonding and electrostatic interactions with the electron-deficient nitrogen atoms of the tetrazine core. These interactions bring the amino acid into close proximity with the emissive cluster–ligand domain, enabling nonradiative deactivation pathways such as excited-state electron or energy

transfer, as well as local perturbation of the ligand-centered excited states. Rather than simple collisional quenching, this behavior is best described as static quenching, arising from the formation of non-emissive host–guest complexes in the ground state. In the low-concentration regime (0–1.25 mM), the Stern–Volmer plot follows a linear relationship, $I_0/I = 891.7$ [Q] + 1.00 ($R^2 = 0.9965$) (Fig. 5b), yielding a Stern–Volmer constant (K_{SV}) of 891.7 M^{-1}. The high linearity and large K_{SV} value indicate strong association between lysine and the framework, consistent with a binding-dominated quenching mechanism. Structurally, this reflects the accessibility of the tetrazine sites within the ladder channels and the favorable electrostatic complementarity between the cationic lysine side chain and the electron-poor tetrazine ring. The calculated limit of detection (LOD) of 407 μM lies within physiologically relevant concentration ranges, highlighting the practical sensitivity of **TUS 9** for lysine monitoring in aqueous systems.

A similar but even more pronounced response was observed for ʟ-arginine. Incremental addition of arginine (0.20–2.89 mM) also produced efficient luminescence quenching (Fig. 5d). The guanidinium group of arginine, which carries a delocalized positive charge and multiple hydrogen-bond donor sites, can engage more strongly with the tetrazine nitrogen atoms than the primary amine of lysine. This enhanced interaction facilitates tighter host–guest association and more efficient excited-state deactivation. In the low-concentration regime (0–0.78 mM), the Stern–Volmer relationship $I_0/I = 540.1$[Q] + 1.00 ($R^2 = 0.9992$) (Fig. 5e) again indicates a static quenching mechanism, with a K_{SV} of 540.1 M^{-1}. Notably, the detection limit for arginine is 162 μM, substantially lower than that for lysine. This enhanced sensitivity likely arises from the stronger multidentate hydrogen-bonding capability and higher charge density of the guanidinium group, which promote more stable binding within the tetrazine-lined microenvironment. From a broader perspective, this result demonstrates how subtle differences in amino acid side-chain chemistry can be amplified by the structured host framework of **TUS 9**, enabling discrimination not only between charged and uncharged species, but also among cationic guests themselves.

In contrast, acidic amino acids exhibit only weak quenching behavior. Addition of ʟ-aspartic acid (0.03–0.61 mM) results in minimal luminescence attenuation (Fig. S12), with a small Stern–Volmer constant of 53.5 M^{-1} (Fig. S13). Similarly, ʟ-glutamic acid (0.07–0.96 mM) shows weak quenching with a K_{SV} of 77.5 M^{-1} (Fig. S14 and S15). The negatively charged $-COO^-$ side chains of these amino acids experience electrostatic repulsion from the electron-rich regions of the tetrazine framework and lack strong hydrogen-bond donor capability. As a result, their association with **TUS 9** is weak and transient, limiting their ability to perturb the emissive states of the silver cluster–linker system.

The pronounced contrast between basic and acidic amino acids highlights a clear structure–activity correlation. In **TUS 9**, the tetrazine linker serves not only as a structural spacer but also as a chemically active recognition element. Its electron-deficient nitrogen atoms create a binding pocket that selec-
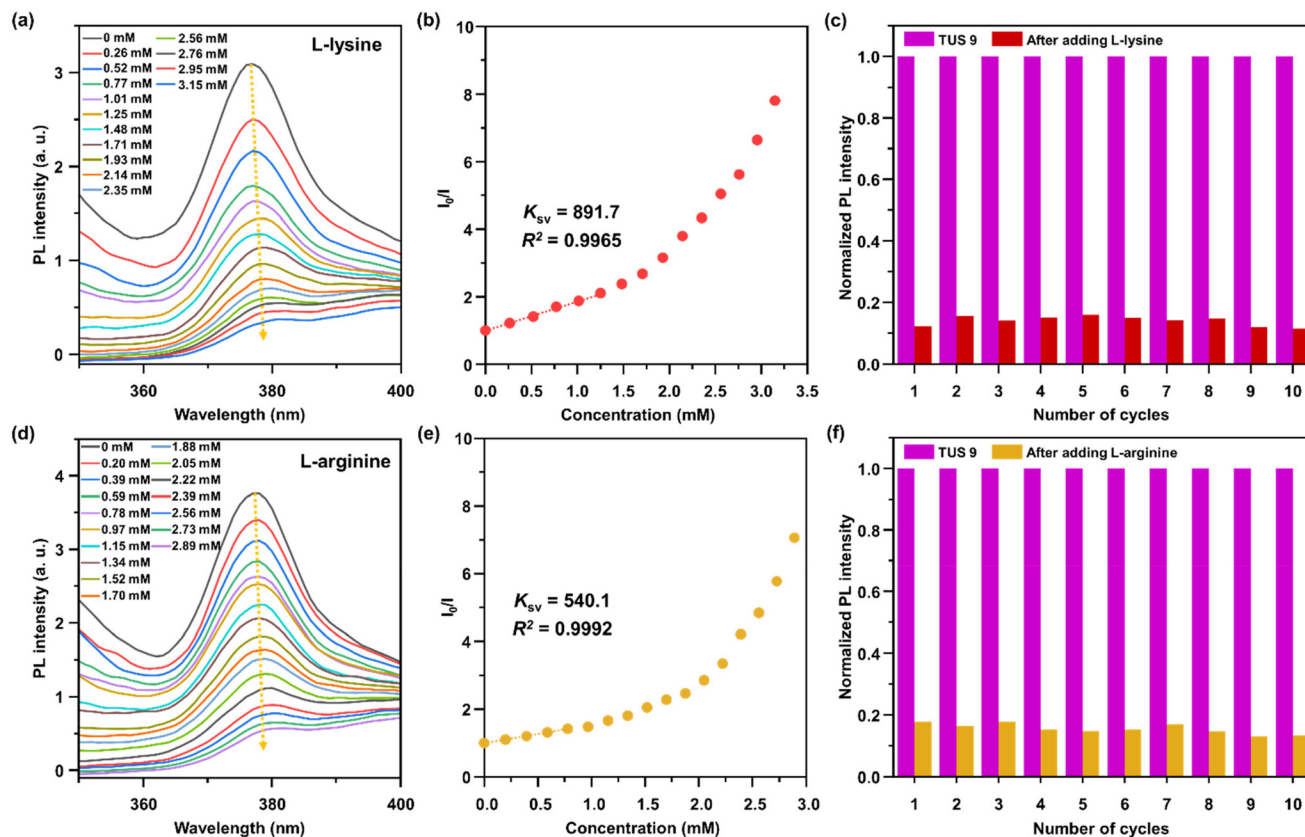
Fig. 5 Concentration-dependent photoluminescence quenching of **TUS 9** upon incremental addition of (a) L-lysine and (d) L-arginine in aqueous media. Corresponding Stern–Volmer plots for (b) L-lysine and (e) L-arginine illustrate the quenching behavior at low analyte concentrations. Recyclability of the luminescence response over multiple sensing–regeneration cycles is shown for (c) L-lysine and (f) L-arginine, demonstrating the operational stability of **TUS 9**.

tively accommodates cationic, hydrogen-bond-donating guests. When lysine or arginine enters this environment, strong host–guest interactions immobilize the amino acid near the emissive domain, promoting nonradiative relaxation pathways that suppress photoluminescence. Acidic amino acids, by contrast, fail to establish such interactions and therefore exert only minor influence on the emission intensity. This selective recognition mechanism transforms the ladder framework into a chemically encoded sensing matrix, where photophysical responses are dictated by molecular complementarity rather than nonspecific adsorption.

Long-term operational stability is a critical requirement for luminescent sensors, particularly in aqueous environments where repeated analyte exposure can degrade frameworks, displace ligands, or alter metal oxidation states. To evaluate the durability of **TUS 9**, recyclability tests were conducted over 10 consecutive sensing–regeneration cycles for both lysine and arginine. For the cycling experiments, L-lysine and L-arginine were used at 3.15 mM and 2.89 mM, respectively (*i.e.*, the maximum concentrations employed in the corresponding titration series), to evaluate operational stability under the most demanding quenching conditions. After each sensing event, the material was isolated, washed with water, and redispersed.

Remarkably, the luminescence quenching response remained essentially unchanged across all cycles (Fig. 5c and f), demonstrating that neither the Ag_{13} cluster chains nor the tetrazine linkers undergo structural or chemical degradation during repeated use. This robustness can be attributed to the rigid, multicoordinated architecture of **TUS 9**. The Ag_{13} clusters are protected by a mixed thiolate–carboxylate shell, while the interchain connectivity is enforced by strong Ag–N coordination to the tetrazine linkers. Together, these interactions create a mechanically and chemically resilient framework that resists ligand exchange, Ag redox processes, and framework collapse in water. Post-sensing XPS analyses further confirm structural preservation. Element-specific spectra collected after lysine exposure (Fig. S16) and arginine exposure (Fig. S17) show no discernible shifts in the binding energies or intensities of Ag, S, N, O, or F signals. This indicates that the oxidation states of silver, the integrity of the thiolate and carboxylate ligands, and the coordination of the tetrazine linkers remain unchanged during sensing. In other words, the luminescence response arises from reversible host–guest interactions rather than from irreversible chemical modification of the framework. Taken together, these results establish **TUS 9** as a reusable luminescent platform that integrates selective

host–guest recognition, sensitive optical response, and exceptional aqueous robustness within a single reticular framework. In this sense, **TUS 9** differs from many solution-phase probes that rely on freely diffusing molecular receptors or dyes, because its emissive and recognition sites are immobilized within a rigid, crystalline nanocluster lattice, enabling stable operation in water and durable performance over repeated sensing–regeneration cycles. This synergy between structural design and photophysical function highlights the broader potential of cluster-assembled frameworks as programmable optical sensors for biologically relevant molecules.

Conclusions

This work demonstrates that the long-standing fragility of Ag NCs can be transformed into an opportunity for functional materials design when structural reinforcement and chemical recognition are integrated at the framework level. By organizing bow-shaped Ag_{13} clusters into 1D chains and subsequently locking these chains into a ladder-like topology using rigid tetrazine-based linkers, we have constructed a SCAM that unites architectural precision, aqueous robustness, and responsive photophysics within a single reticular platform. The resulting framework, **TUS 9**, preserves its crystallinity, coordination environment, and luminescence under aqueous conditions—an essential prerequisite for realistic sensing applications. Beyond structural stabilization, the tetrazine linker plays an active chemical role by introducing an electronically and supramolecularly programmable recognition site. Its electron-deficient nitrogen-rich core selectively engages cationic amino acids through hydrogen bonding and electrostatic interactions, positioning guest molecules in close proximity to the emissive cluster–ligand domain. This targeted host–guest coupling enables efficient modulation of excited-state relaxation pathways, producing strong and selective luminescence quenching responses toward L-lysine and L-arginine while largely excluding acidic amino acids. Importantly, the sensing behavior is fully reversible and reproducible, underscoring the chemical resilience of the Ag_{13} chain scaffold and the robustness of the Ag–N, Ag–S, and Ag–O coordination network. Conceptually, this study highlights how linker design in cluster-based reticular materials can transcend a purely structural role and instead serve as a molecular interface between framework stability and chemical function. By embedding electronically active and recognition-capable motifs directly into the backbone of a silver cluster lattice, it becomes possible to encode selectivity, sensitivity, and durability into the same material platform. Such an approach moves beyond conventional strategies that treat luminescence, stability, and molecular recognition as independent design challenges. More broadly, the ladder-structured architecture of **TUS 9** illustrates how hierarchical cluster organization—clusters to chains, chains to frameworks—can be exploited to generate confined yet accessible microenvironments for analyte interaction in water. This opens new directions for using silver nanoclusters not merely as discrete

emitters, but as building blocks for programmable photonic solids capable of chemical discrimination. The principles established here should be extendable to other functional linkers, cluster nuclearities, and target analytes, offering a versatile blueprint for the development of next-generation luminescent materials for bioanalysis, environmental monitoring, and molecular diagnostics.

Author contributions

Conflicts of interest

There are no conflicts to declare.

Data availability

The data supporting this article have been included as part of the supplementary information (SI). Supplementary information is available. See DOI: https://doi.org/10.1039/d6nr00302h.

CCDC number 2523357 (**TUS 9**) contain the supplementary crystallographic data for this paper.[72]

Acknowledgements

References

1 Y. Du, H. Sheng, D. Astruc and M. Zhu, *Chem. Rev.*, 2020, **120**, 526–622.

2 X. Kang and M. Zhu, *Chem. Soc. Rev.*, 2019, **48**, 2422–2457.

3 S. Li, N.-N. Li, X.-Y. Dong, S.-Q. Zang and T. C. W. Mak, *Chem. Rev.*, 2024, **124**, 7262–7378.

4 Z. Yang, Y. Wang, R. Zhang, T. Chen and J. Xie, *Adv. Mater.*, 2025, **37**, e08578.

5 H. Lin, X. Song, O. J. H. Chai, Q. Yao, H. Yang and J. Xie, *Adv. Mater.*, 2024, **36**, 2401002.

6 K. L. D. M. Weerawardene, H. Häkkinen and C. M. Aikens, *Annu. Rev. Phys. Chem.*, 2018, **69**, 205–229.

7 R. Jin, C. Zeng, M. Zhou and Y. Chen, *Chem. Rev.*, 2016, **116**, 10346–10413.

8 R. Jin, G. Li, S. Sharma, Y. Li and X. Du, *Chem. Rev.*, 2021, **121**, 567–648.

9 I. Chakraborty and T. Pradeep, *Chem. Rev.*, 2017, **117**, 8208–8271.

10 R. K. Gupta, Z. Wang, B. Mohan, C.-H. Tung and D. Sun, *Adv. Funct. Mater.*, 2025, 2507047.

11 H. Hirai, S. Ito, S. Takano, K. Koyasu and T. Tsukuda, *Chem. Sci.*, 2020, **11**, 12233–12248.

12 H. Seong and D. Lee, *Bull. Korean Chem. Soc.*, 2024, **45**, 435–450.

13 S. Maity, S. Kolay, S. Chakraborty, A. Devi, Rashi and A. Patra, *Chem. Soc. Rev.*, 2025, **54**, 1785–1844.

14 Y. Lu and W. Chen, *Chem. Soc. Rev.*, 2012, **41**, 3594–3623.

15 P. D. Jadzinsky, G. Calero, C. J. Ackerson, D. A. Bushnell and R. D. Kornberg, *Science*, 2007, **318**, 430–433.

16 L. C. McKenzie, T. O. Zaikova and J. E. Hutchison, *J. Am. Chem. Soc.*, 2014, **136**, 13426–13435.

17 Z. Gan, J. Chen, J. Wang, C. Wang, M.-B. Li, C. Yao, S. Zhuang, A. Xu, L. Li and Z. Wu, *Nat. Commun.*, 2017, **8**, 14739.

18 M. Brust, M. Walker, D. Bethell, D. J. Schiffrin and R. Whyman, *J. Chem. Soc., Chem. Commun.*, 1994, 801–802.

19 Y. Xiao, Z. Wu, Q. Yao and J. Xie, *Aggregate*, 2021, **2**, 114–132.

20 L. Zhang and E. Wang, *Nano Today*, 2014, **9**, 132–157.

21 K. Sahoo, T. R. Gazi, S. Roy and I. Chakraborty, *Commun. Chem.*, 2023, **6**, 157.

22 Q. Shi, Z. Qin, S. Sharma and G. Li, *Chem. Rec.*, 2021, **21**, 879–892.

23 J.-Q. Fan, J.-X. Guo and M.-B. Li, *Chem. – Eur. J.*, 2025, **31**, e02620.

24 Q. Li, B. Huang, S. Yang, J. Chai, Y. Pei and M. Zhu, *Aggregate*, 2025, **6**, e70222.

25 T.-H. Chen and W.-L. Tseng, *Small*, 2012, **8**, 1912–1919.

26 S. Sharma, K. Kaushik, A. Salam, R. Garg, J. Mondal, R. Lamba, M. Kaur and C. K. Nandi, *ACS Appl. Nano Mater.*, 2024, **7**, 32–60.

27 L. Chen, A. Black, W. J. Parak, C. Klinke and I. Chakraborty, *Aggregate*, 2022, **3**, e132.

28 T. Xu, B. Xiang, Y. Chen, Y. Wang, Y. Song and R. Jin, *JACS Au*, 2025, **5**, 5286–5311.

29 A. Baghdasaryan and H. Dai, *Chem. Rev.*, 2025, **125**, 5195–5227.

30 V. Truttmann, A. Loxha, R. Banu, E. Pittenauer, S. Malola, M. F. Matus, Y. Wang, E. A. Ploetz, G. Rupprechter, T. Bürgi, H. Häkkinen, C. Aikens and N. Barrabés, *ACS Nano*, 2023, **17**, 20376–20386.

31 I. Dolamic, S. Knoppe, A. Dass and T. Bürgi, *Nat. Commun.*, 2012, **3**, 798.

32 H. Zhu, Z. Wang, Q. Yao, P. Zhang, J. Xie and X. Yuan, *Adv. Funct. Mater.*, 2026, **36**, e07924.

33 Q. Chen, J. Chen, Z. Yang, L. Zhang, Z. Dong and Z. Liu, *Nano Res.*, 2018, **11**, 5657–5669.

34 S. Biswas, T. Tanaka, H. Song, M. Ogami, Y. Shingyouchi, S. Hossian, M. Kamiyama, T. Kosaka, R. Nakatani, Y. Niihori, S. Das, T. Kawawaki, D.-e. Jiang and Y. Negishi, *Small Sci.*, 2025, **5**, 2400465.

35 X. Gu, J. Zhang, S. Guo, Y. Zhang, L. Xu, R. Jin and G. Li, *J. Am. Chem. Soc.*, 2025, **147**, 22785–22795.

36 Y. Jin, C. Zhang, X.-Y. Dong, S.-Q. Zang and T. C. W. Mak, *Chem. Soc. Rev.*, 2021, **50**, 2297–2319.

37 Z. Wang, R. K. Gupta, G.-G. Luo and D. Sun, *Chem. Rec.*, 2020, **20**, 389–402.

38 I. Díez and R. H. A. Ras, *Nanoscale*, 2011, **3**, 1963–1970.

39 X. Liu, T. Ki, G. Deng, S. Yoo, K. Lee, B.-H. Lee, T. Hyeon and M. S. Bootharaju, *Nanoscale*, 2024, **16**, 12329–11234.

40 Y.-P. Xie, Y.-L. Shen, G.-X. Duan, J. Han, L.-P. Zhang and X. Lu, *Mater. Chem. Front.*, 2020, **4**, 2205–2222.

41 S. Biswas, P. Sun, X. Xin, S. Mandal and D. Sun, Chapter 15 – Atom-Precise Cluster-Assembled Materials, in *Atomically Precise Nanochemistry*, ed. R. Jin and D. Jiang, John Wiley & Sons Ltd, Chichester, 2023, pp. 453–478. DOI: 10.1002/9781119788676.ch15.

42 X. Kang and M. Zhu, *Coord. Chem. Rev.*, 2019, **394**, 1–38.

43 Y.-P. Xie, J.-L. Jin, G.-X. Duan, X. Lu and T. C. W. Mak, *Coord. Chem. Rev.*, 2017, **331**, 54–72.

44 Z. Wang, X.-Y. Li, L.-W. Liu, S.-Q. Yu, Z.-Y. Feng, C.-H. Tung and D. Sun, *Chem. – Eur. J.*, 2016, **22**, 6830–6836.

45 S. A. Claridge, A. W. Castleman Jr., S. N. Khanna, C. B. Murray, A. Sen and P. S. Weiss, *ACS Nano*, 2009, **3**, 244–255.

46 O. M. Yaghi, M. J. Kalmutzki and C. S. Diercks, *Introduction to Reticular Chemistry: Metal–Organic Frameworks and Covalent Organic Frameworks*, Wiley-VCH, Weinheim, Germany, 2019.

47 S. Biswas, S. Das and Y. Negishi, *Coord. Chem. Rev.*, 2023, **492**, 215255.

48 R. Nakatani, S. Das and Y. Negishi, *Nanoscale*, 2024, **16**, 9642–9658.

49 N. Alam, A. K. Das, P. Chandrashekar, P. Baidya and S. Mandal, *Nanoscale*, 2024, **16**, 10087–10107.

50 Z.-Y. Wang and S.-Q. Zang, Chapter 16 – Coinage Metal Cluster-Assembled Materials, in *Atomically Precise Nanochemistry*, ed. R. Jin and D. Jiang, John Wiley & Sons Ltd, Chichester, 2023, pp. 479–501. DOI: 10.1002/9781119788676.ch16.

51 R.-W. Huang, Y.-S. Wei, X.-Y. Dong, X.-H. Wu, C.-X. Du, S.-Q. Zang and T. C. W. Mak, *Nat. Chem.*, 2017, **9**, 689–697.

52 Z.-Y. Wang, M.-Q. Wang, Y.-L. Li, P. Luo, T.-T. Jia, R.-W. Huang, S.-Q. Zang and T. C. W. Mak, *J. Am. Chem. Soc.*, 2018, **140**, 1069–1076.

53 M. Cao, R. Pang, Q.-Y. Wang, Z. Han, Z.-Y. Wang, X.-Y. Dong, S.-F. Li, S.-Q. Zang and T. C. W. Mak, *J. Am. Chem. Soc.*, 2019, **141**, 14505–14509.

54 A. K. Das, S. Biswas, A. Thomas, S. Paul, A. S. Nair, B. Pathak, M. S. Singh and S. Mandal, *Mater. Chem. Front.*, 2021, **5**, 8380–8386.

55 J. Sakai, K. Sasaki, R. Nakatani, S. Das and Y. Negishi, *Nanoscale*, 2024, **16**, 21767–21775.

56 R. Nakatani, S. Biswas, T. Irie, Y. Niihori, S. Das and Y. Negishi, *ACS Mater. Lett.*, 2024, **6**, 438–445.

57 Z. Chang, X. Jing, C. He, X. Liu and C. Duan, *ACS Catal.*, 2018, **8**, 1384–1391.

58 J.-Y. Wang, W.-H. Li, Z. Wei, C. Zhang, Y.-H. Li, X.-Y. Dong, G. Xu and S.-Q. Zang, *Chem. Commun.*, 2020, **56**, 2091–2094.

59 Q.-X. Zang, Z.-Y. Wang, Y. Li, X.-M. Luo, H.-Y. Li, Y.-N. Si and S.-Q. Zang, *Chem. Commun.*, 2022, **58**, 11985–11988.

60 X.-Y. Dong, Y. Si, J.-S. Yang, C. Zhang, Z. Han, P. Luo, Z.-Y. Wang, S.-Q. Zang and T. C. W. Mak, *Nat. Commun.*, 2020, **11**, 3678.

61 J.-Y. Wang, Y. Si, X.-M. Luo, Z.-Y. Wang, X.-Y. Dong, P. Luo, C. Zhang, C. Duan and S.-Q. Zang, *Adv. Sci.*, 2023, **10**, 2207660.

62 R. Nakatani, S. Biswas, T. Irie, J. Sakai, D. Hirayama, T. Kawawaki, Y. Niihori, S. Das and Y. Negishi, *Nanoscale*, 2023, **15**, 16299–16306.

63 J. Sakai, S. Biswas, T. Irie, H. Mabuchi, T. Sekine, Y. Niihori, S. Das and Y. Negishi, *Nanoscale*, 2023, **15**, 12227–12234.

64 T. Irie, K. Sasaki, M. Nozaki, T. Kawawaki, S. Takahashi, S. Das and Y. Negishi, *Nanoscale*, 2025, **17**, 25495–25504.

65 M. Cao, S. Wang, J.-H. Hu, B.-H. Lu, Q.-Y. Wang and S.-Q. Zang, *Adv. Sci.*, 2022, **9**, 2103721.

66 Y.-H. Li, R.-W. Huang, P. Luo, M. Cao, H. Xu, S.-Q. Zang and T. C. W. Mak, *Sci. China:Chem.*, 2019, **62**, 331–335.

67 A. K. Das, S. Biswas, S. S. Manna, B. Pathak and S. Mandal, *Inorg. Chem.*, 2021, **60**, 18234–18241.

68 M. J. Alhilaly, R.-W. Huang, R. Naphade, B. Alamer, M. N. Hedhili, A.-H. Emwas, P. Maity, J. Yin, A. Shkurenko, O. F. Mohammed, M. Eddaoudi and O. M. Bakr, *J. Am. Chem. Soc.*, 2019, **141**, 9585–9592.

69 J.-Y. Wang, J.-W. Yuan, X.-M. Liu, Y.-J. Liu, F. Bai, X.-Y. Dong and S.-Q. Zang, *Aggregate*, 2024, e508.

70 M. Zhao, S. Huang, Q. Fu, W. Li, R. Guo, Q. Yao, F. Wang, P. Cui, C.-H. Tung and D. Sun, *Angew. Chem., Int. Ed.*, 2020, **59**, 20031–20036.

71 Z. Wang, Y.-J. Zhu, Y.-Z. Li, G.-L. Zhuang, K.-P. Song, Z.-Y. Gao, J.-M. Dou, M. Kurmoo, C.-H. Tung and D. Sun, *Nat. Commun.*, 2022, **13**, 1802.

72 CCDC 2523357: Experimental Crystal Structure Determination, 2026, DOI: 10.5517/ccdc.csd.cc2qprmt.